J2.4 **AN AUTOMATED METHOD FOR DETECTING PRECIPITATION AND CELL TYPE FROM RADAR PRODUCTS**

George L. Limpert[1], Steven A. Lack[2], Neil I. Fox[1], and E. John Sadler[3]

University of Missouri-Columbia, Columbia, Missouri[1]
NOAA/ESRL/GSD/CIRES University of Colorado, Boulder, Colorado[2]
USDA-ARS Cropping Systems and Water Quality Research Unit, Columbia, Missouri[3]

1. INTRODUCTION

It is of interest for many purposes, including nowcasting, to evaluate the structure of radar images in an effort to produce more accurate estimates of rainfall totals from radar data. Although subjective analysis can reliably determine the structure of radar imagery, computational techniques exist to analyze a radar image using algorithms that can be automated. Many of these techniques use some form of multiresolution analysis or Fourier analysis to accomplish structure identification.

One method of identifying structures of differing sizes and scales within an image is to use high, low, and band pass filters to highlight features of interest. This is frequently accomplished by decomposing an image into the frequency domain using a transform and performing the filtering operation within the frequency domain. A variety of transforms exist for accomplishing this including the Wavelet Transform (WT) and many transforms related to the Fourier Transform (FT).

An algorithm, based on the FT and Gaussian filters, has been developed to analyze a radar image and identify structures within the image. A variety of cases are then presented to demonstrate the performance and robustness of this algorithm. Primarily this algorithm delineates regions of convective and stratiform precipitation and identifies convective structures on multiple scales. Properties of convective features are also determined by the algorithm including finding a centroid and attempting to fit an ellipse to define the structure. Additional properties of convective features are determined within the classification scheme.

* *Corresponding Author Address:* George L. Limpert, 302 ABNR Bldg., Univ. of Missouri-Columbia, Dept. of Soil, Environmental, and Atmospheric Science, Columbia, MO, 65211; E-mail: gll883@mizzou.edu

2. FOURIER TRANSFORM

The FT decomposes a signal in the spatial domain into a linear combination of sinusoidal orthonormal basis functions, which are represented in the frequency domain. Mathematically, the Continuous Fourier Transform (CFT) can be expressed in a single dimension as (1),

$$F(u) = \int_{-\infty}^{\infty} f(x)e^{-2\pi iux}dx \qquad (1)$$

which produces sinusoidal waves as shown by Euler's Formula. A corresponding similar equation, the Inverse Fourier Transform (IFT), exists to recompose the signal from the frequency domain into the spatial domain.

There are a number of implicit assumptions of the FT. These include that the signal is periodic and the pattern observed in the spatial domain is due entirely to patterns of constructive and destructive interference. That is to say that the power of a given frequency remains constant throughout the entire domain. Although these assumptions may not be realistic, the FT is still suitable for analyzing a signal.

When computing the FT, a signal is sampled at discrete intervals, and a similar pair of equations known as the Discrete Fourier Transform (DFT) and Inverse Discrete Fourier Transform (IDFT) are used. If computed by solving the equation for each (u), or (u,v) if in two dimensions, the computation will be of $O(n^2)$, which may not be feasible for large domains. Instead, the FT is calculated using the Fast Fourier Transform (FFT), which is of the complexity $O(n \log n)$, and can be computed more readily even when the domain is large.

The FT, along with similar transforms, can be used in multiple dimensions. The FT, and other related transforms, can be used for image processing and compression applications. The signal is decomposed into a linear combination of orthonormal basis images.

One important property in Fourier analysis and synthesis is the Convolution Theorem. The theorem states that convolution and multiplication are related between the spatial domain and frequency domain. Convolution in one domain corresponds to multiplication in the other domain.

3. SIGNAL FILTERING

Although many filters exist for filtering signals, including ideal filters and Butterworth filters, the research herein will focus on Gaussian filters. In this context, filtering refers to attenuating or boosting a component of a signal based on the frequency of the component. As it might appear, this can be accomplished through multiplication in the frequency domain. By the Convolution Theorem, filtering would be accomplished in the spatial domain through convolution.

A low pass filter attenuates high frequency components of a signal while retaining lower frequency components. In two dimensions, the Gaussian function is given by (2),

$$G(u,v) = \frac{1}{2\pi\sigma^2} e^{-\frac{u^2+v^2}{2\sigma^2}} \qquad (2)$$

and is multiplied by the signal in the frequency domain to perform a Gaussian filtering operation. A high pass filter attenuates low frequency components of a signal and retains the higher frequency components. The portion of a signal attenuated by a low pass filter is the same as the portion of a signal retained by a high pass filter. A band pass filter retains components within a range of frequencies while attenuating signals with frequencies above and below the range. This can be performed through a low pass filter to remove signals below the low cutoff frequency followed by a high pass filter to remove signals above the high cutoff frequency.

4. SPATIAL ANALYSIS OF PRECIPITATION

Previous work has been done in analyzing the spatial characteristics of rainfall. Much of this work has been done for the purposes of developing nowcasting systems. Some nowcasting systems decompose an image into various spatial scales using the FT with the purpose of advecting or evolving features of different scales at least partially independent of other scales.

Seed (2003) devised the Spectral Prognosis (S-PROG) nowcasting scheme which uses the FT and band pass filtering to produce pseudo-reflectivity radar images. In this scheme, the FT decomposes a radar image into the frequency domain and the image is then filtered in the frequency domain into multiple scales using a Gaussian band pass filter. In addition to forecasting based on advection, high frequency features are attenuated more rapidly than low frequency features because high frequency features are more transient and therefore are less predictable.

Precipitation systems can be classified based on reflectivity gradients. Klazura et al. (1999) characterized precipitation systems into four categories based on the temporal evolution of the systems and horizontal gradients in reflectivity within the systems. The categories were systems that had high reflectivity gradients, systems that began with high reflectivity gradients and transitioned to lower reflectivity gradients through the life of the system, systems with high reflectivity gradients embedded within lower reflectivity gradients, and systems with low reflectivity gradients. Systems with high reflectivity gradients were noted to have small cores with reflectivity power of 40 to 60 dBZ with high reflectivity gradients around the core. In systems with lower reflectivity gradients, weaker reflectivity power of 25 to 40 dBZ was noted over a more widespread area.

Hagelberg and Helland (1995) used a variation of the Morlet Wavelet in two dimensions to detect radar thinlines. The wavelet function is symmetric and directionally selective. Application of the wavelet at different directions and scales was done. Areas where strong power is present in the output of the transform suggest the presence of a possible thinline. The WT is similar in nature to the FT in that it decomposes an image in the spatial domain into frequency bands. However, unlike the FT, the power in a given frequency is not fixed across the entire domain. Power can be localized in portions of the domain in a frequency band. Multiscale analysis can be accomplished by either downsampling the image or by scaling the wavelet function. Wavelets may also be useful to analyze radial velocity images for tornado vortex signatures (Liu et al. 2007) and to analyze oceanic velocity data derived from sea surface height maps for vortexes (Turiel et al. 2007).

5. METHODOLOGY

Several cases have been chosen to demonstrate the

performance of the algorithm under a variety of conditions. These cases are examined using subjective analysis and then are processed using the algorithm to objectively analyze the image. The algorithm used relies only on radar-derived products with no knowledge of the environmental conditions producing the structures observed by radar. Although using additional data such as model derived parameters may provide for a better interpretation, whether subjective or automated, only radar-derived products are used for demonstrating the concept.

A primary use of the algorithm is to distinguish convective and stratiform precipitation. Cases of pure stratiform precipitation, pure convective precipitation, and stratiform precipitation with convective elements are chosen. In cases with convective precipitation, it is useful to identify structures within the image of different scales. For example, individual cells may be embedded within a larger complex, such as individual thunderstorm cells within a squall line. However, there are also cases with scattered or isolated thunderstorm activity in which individual cells are not contained within larger complexes. To test the performance of the algorithm, cases with isolated cells and with thunderstorm complexes are chosen as well.

Algorithms within the Warning Decision Support System – Integrated Information (WDSS-II) software (Lakshmanan et al. 2007) are used to prepare radar data for use within the algorithm. The ldm2netcdf algorithm is used to ingest level II data and convert it to the Network Common Data Form (NetCDF) format. The w2merger algorithm (Lakshmanan et al. 2006) is used to produce a latitude-longitude-height grid from the radar data, which is on a polar grid. Data from a single radar is used to generate the grid, which has a grid point spacing of 1 km horizontally and vertically, a size of 256 km by 256 km horizontally, and is centered on the radar site. Reflectivity at an elevation of 3 km is used in the algorithm because lower elevations have missing data at the edges of the grid.

6. ALGORITHM DESCRIPTION

The crux of the classification scheme involves decomposing a radar image to identify structures of different scales within the image. This is accomplished through the DFT, applying various Gaussian low pass, band pass, and high pass filters within the frequency domain, and recomposing the filtered images into the spatial domain. Examining the filtered images yields information about how much power is within an image at each point within the selected frequency band.

Identification of convective and stratiform structures is done independently. That is to say that a region of the image may be identified both as being convective and stratiform. This is realistic because convection is frequently embedded within larger systems that contain stratiform precipitation. Stratiform precipitation occurs on a lower frequency and may contain higher frequency signals indicating embedded convection.

6.1. Precipitation Classification

Stratiform precipitation is identified as areas that meet two criteria. The reflectivity of the original image at the point identified must be at or above 10 dBZ. At least 5 dBZ must be concentrated within a selected low frequency band.

Convective precipitation is also identified by two criteria. Power is determined by summing the weighted power within three frequency bands. If the power is above a certain reflectivity threshold and the reflectivity from the original image is above a threshold as well, the point is marked as convective. If reflectivity within the original image is weak, a strong signal within the bands used for identifying convection is required to mark the point as convective. Conversely, if reflectivity within the original image is strong, a weaker signal within the bands for identifying convection is required to mark the point as convective. If reflectivity in the original image exceeds the hail cap (53 dBZ in this scheme) the point is marked as convective regardless of the power within frequency bands.

To determine convection, two values are compared against a series of thresholds. One of the values, signal strength within bands used for identifying convection, is computed by weighting and summing power within three bands. Values of σ given in the equation are based on a square domain with a length of 256 km and a grid point spacing of 1 km. The first subscript is the lower cutoff frequency and the second subscript is the higher cutoff frequency of the band. This value is calculated by (3),

$$R_{bpf}(x,y) = B_{3,12} + B_{12,30} + \frac{B_{1,4}}{2} \qquad (3)$$

and is used to represent the signal in bands that would

represent convection. The other value is based on reflectivity within the original image. Table 1 shows the thresholds for R_{bpf} and R used for identifying convection. If the criteria are both satisfied, the point is marked as convective.

R Threshold	R_{bpf} Threshold
≥ 7 dBZ	≥ 25 dBZ
≥ 16 dBZ	≥ 20 dBZ
≥ 25 dBZ	≥ 15 dBZ
≥ 34 dBZ	≥ 10 dBZ
≥ 43 dBZ	≥ 5 dBZ
≥ 53 dBZ	N/A

Table 1: *Thresholds used for identifying convection*

Additional echoes stronger than 5 dBZ that have not been identified as convective or stratiform are additionally marked. Although these echoes are not classified as precipitation, they may be useful in identifying other structures such as boundaries along which strong convergence is occurring.

An attempt is made to classify embedded convection within larger stratiform structures. Such regions must be classified both as convective and stratiform by the previous classification scheme. Additionally, criteria must be met so that ratios of power in frequency bands associated with convection compared to power in bands associated with convection is below a threshold. The purpose of this is to require that, although the region is classified as convective and stratiform, the stratiform signal is relatively strong compared to the convective signal. Without these additional criteria, it is likely that many larger convective systems would meet both the convective and stratiform requirements and would have large areas classified as embedded convection that would likely not be classified as embedded convection in a subjective analysis by a forecaster.

6.2. Structure Identification

The cluster, segment, and cell identification schemes work by identifying structures of different scales within an image. Structures of different scales may be contained within one another to represent a hierarchy of structures within a reflectivity image. That is to say a cluster may

contain multiple segments, each of which may contain multiple cells. Segments are not required to be contained within clusters and cells are not required to be contained within segments or clusters. Clusters are not required to contain segments or cells and segments are not required to contain cells. Each scale is identified independently of other scales.

As with the convective and stratiform identification scheme, each cluster, segment, and cell must meet a series of criteria for that scale. Clusters, segments, and cells must consist entirely of points that have been marked as convective. Other power thresholds within frequency bands must also be satisfied to meet each classification. Cluster identification only examines power within the lowest frequency band associated with convection whereas segment and cell identification examine progressively higher frequency bands.

Upon tagging clusters, segments, and cells, additional filtering is performed to remove very small structures at each scale. To accomplish this, the image is eroded and dilated using the same mask, which can be defined separately for each scale if desired. By specifying larger masks, larger structures will be removed. This not only has the effect of removing structures that are smaller than the mask, but also of removing detail around the edges of structures.

To identify structures within a scale, the filtered image is examined for points within a structure. When a point in a structure is identified within the filtered image, a scanline fill is performed starting from the identified point, but the fill is performed within the unfiltered image. This identifies only structures present within the filtered image, however, the structures retain their shape from the unfiltered image. Small structures are removed by the filtering operation while larger structures remain unaltered by the filtering operation.

6.3. Shape Determination

A variety of metrics are computed on the clusters, segments, and cells once they have been identified. Three simple metrics computed are the area of the structure, the maximum reflectivity power within the structure, and the average reflectivity of the structure.

It is of interest to determine a centroid of a structure, which is useful in some shape analysis algorithms. The centroid is determined by computing a penalty function for every point within the structure. The point for which

the penalty is lowest is determined to be the centroid. The algorithm for finding the centroid attempts to place the centroid near the spatial center of the structure but also near the core as indicated by the strongest reflectivity within the structure (reflectivity-weighted centroid). The penalty function is computed by summation of (4),

$$P(x, y) = R(x, y) \times D \qquad (4)$$

where R is the reflectivity at (x,y) and D is the distance from (x,y) to the centroid for all (x,y) within the cell. The penalty function is computed for all points within the structure. The point where the penalty function is minimized is determined to be the centroid. The centroid must be within the structure, regardless of the shape of the structure. The reflectivity at the centroid of the structure is computed as another metric.

Edge detection is used within the shape analysis to approximate the shape of the structure. The best method for identifying structure edges is to consider four directions adjacent to a pixel, which are north, south, east, and west. For a point within a structure, it is on the edge of a structure if at least one of the pixels in one of the four adjacent directions directly next to the pixel is not in the structure. Also, if at least one of the four neighboring pixels is not within the domain, the pixel is considered to be at the edge of the structure. This is typically sufficient for detecting the edge of a structure. However, for the purposes of shape analysis, if any of the eight directly neighboring pixels to a pixel are not part of the structure, the pixel is considered to be an edge.

Although there are many methods for representing the shape of a structure, a simple method that is useful in shape analysis is to approximate the structure as an ellipse. An ellipse can be represented by a center point, major axis, and minor axis.

From the centroid, the distance to each point that is considered to be an edge is computed. The line through the centroid to the most distant edge point from the centroid is considered to be the major axis of the ellipse. From the centroid, the most distant edge point perpendicular to the major axis is considered to be the minor axis of the ellipse. By adding 0.5 to the length of the major axis in pixels and dividing by the length of the minor axis plus 0.5, eccentricity can be computed. It is possible, using this method of computing the shape of the cell, to have a minor axis of length zero. Depending on the shape of a cell and the position of the centroid, it is possible for the minor axis to be zero pixels in length.

Division by zero when computing the eccentricity is prevented by adding 0.5 to both the length of the minor axis and the length of the major axis so that neither axis can ever have a length of zero.

7. CASES SELECTED AND RESULTS

Several cases of varying types are selected to demonstrate the robustness of the classification scheme used. Subjective analysis of each of the cases is compared with the objective analysis performed by the algorithm.

The ten cases were prepared and processed using the algorithm described previously. Each case will be discussed independently with analysis of the performance of the algorithm. In the images, each cell, segment, and cluster is uniquely colored. In images showing the classification of precipitation types, dark red indicates convection, with other colors indicating stratiform precipitation, other echoes above 5 dBZ, and no precipitation as the color scale progresses to blue.

1) KEAX at 2000 UTC on March 12, 2006

Shown in figure 1a, several supercells are evident in the image with three distinct clusters of cells. Some of the clusters contain three or four cells. In addition to the several reflectivity cores, weak echoes are noted to the east of the cores, likely associated with thunderstorm anvils.

As shown in figure 1b, the algorithm correctly identified the intense reflectivity cores as convective in nature. The structures detected by the algorithm are shown in figures 1c through 1e. There are several distinct cells in the image, which seem to correspond well to the cells identified by the algorithm. Three distinct clusters are identified by the algorithm, which seems reasonable. Even though precipitation was not occurring in the areas beneath the thunderstorm anvils, the algorithm is not provided information as to the vertical extent of the structures. Identifying those regions as stratiform precipitation is reasonable given the information provided to the algorithm. The algorithm performs well in this case both on discriminating convective and stratiform precipitation and identifying structures at multiple scales.

2) KMLB at 1100 UTC on February 2, 2007

A line of supercells is present in the image, shown in figure 2a, with additional isolated to scattered convection just ahead of the line, to the north of the line, and to the southwest of the line. Weak echoes are noted to the southeast of many of the thunderstorms, likely present as a result of thunderstorm anvils.

The convection in the image is properly classified by the algorithm in figure 2b. Figures 2c through 2e show the structures present at the spatial scales examined. Although the convective precipitation is correctly identified, it would appear that there are more cells than are identified individually by the algorithm. Several of the cells that are identified have an elongated appearance, which is due to the presence of multiple cells located adjacent to one another that are being identified as a single cell. Although one of the clusters identified appears too small to actually qualify as a cluster, three other distinct clusters of cells apparent in the radar image are correctly identified by the algorithm. Convective and stratiform precipitation are identified well by the algorithm. The algorithm performs moderately well at identifying features at multiple scales.

3) KILX at 2100 UTC on July 13, 2004

In figure 3a, two large clusters of thunderstorms are evident in the radar image. The northwestern cluster has several distinct reflectivity cores embedded within it. The southeastern cluster is at the edge of the domain and the structure is less clear. Scattered thunderstorm cells are also present to the northwest of the clusters and between the clusters. Weak echoes are present to the south and northeast of the clusters, likely associated with thunderstorm anvils.

The identification of convective and stratiform precipitation, shown in figure 3b, by the algorithm appears to be reasonable. Figures 3c through 3e show the structures present at the spatial scales examined. Although one of the clusters that is identified appears to be small enough to not qualify as a cluster, the other two clusters are identified correctly. The identification of convective cells within the clusters appears mostly reasonable. It is difficult to subjectively discern cells within some portions of the clusters, so it is reasonable that some portions of clusters do not have cells identified within them. Overall, the performance of identifying convective precipitation is good. However, the algorithm performs moderately well at identifying features at multiple scales.

4) KSGF at 0230 UTC on June 21, 2000

As shown in figure 4a, a line of thunderstorms with embedded cells extends across the domain oriented from the west-southwest to the east-northeast. Scattered convection is occurring to the south of the line of thunderstorms. Weaker echoes are noted to the north of the line likely due to thunderstorm anvils and stratiform precipitation.

The identification of the line of thunderstorms and isolated cells as convective with much of the precipitation to the north of the line identified as stratiform seems reasonable. Convective and stratiform areas are shown in figure 4b. Figures 4c through 4e show the structures present at the spatial scales examined. Although numerous cells are properly identified within the line, there are many more that are not identified. Identification of segments and clusters was better. However, there are clusters identified that are too small to be subjectively identified as a cluster. The algorithm performed well at identifying convective and stratiform precipitation. The performance of identifying features at multiple scales was moderately good.

5) KSGF at 2230 UTC on January 12, 2005

Figure 5a shows a broken line of thunderstorms extends across much of the domain from south-southwest to north-northeast. The thunderstorm activity is embedded within a larger region of weaker echoes likely due to thunderstorm anvils and stratiform precipitation. Some evidence of a melting layer is evident in the image. Scattered convective cells and some weaker echoes are present to the east of the line in the southern portion of the image. Additional convective cells are present in the northwest corner of the image embedded within some weaker echoes likely due to thunderstorm anvils and stratiform precipitation.

In figure 5b, he algorithm appears to identify a few regions of the image as convective that may not be convective in nature. However, regions that should be identified as convective appear to be properly identified. Figures 5c through 5e show the structures present at the spatial scales examined. There are a few cells within the image that are not identified. The algorithm appeared to perform better at identifying segments and clusters,

however. The algorithm performed moderately well both at identifying convection and identifying features at multiple scales within the image.

6) KSGF at 2330 UTC on April 22, 2004

Shown in figure 6a, scattered thunderstorms are noted throughout much of the southwest and northeast corners of the image. A region of weaker reflectivity is noted extending east from two cells located in the far southwest corner of the image, likely due to thunderstorm anvils from the cells.

Although there may be a couple of false positives in identifying convection within the image, shown in figure 6b, overall the performance is quite good. Figures 6c through 6e show the structures present at the spatial scales examined. Cells within the image are mainly discrete, and the identification appears to be quite good. Because the cells are discrete but somewhat large in size, it seems reasonable that they are also identified as segments and sometimes as clusters. Both the identification of convective and stratiform precipitation and the identification of features at multiple scales appears to be quite good in this case.

7) KEAX at 0600 UTC on December 1, 2006

In figure 7a, a large region of weak echoes associated with stratiform precipitation extends over all but the far western and northwestern part of the radar image. The precipitation is mainly in the form of snow with possibly sleet and freezing rain in the southern and eastern part of the image. A band of stronger reflectivity extends east-northeast from nearly the center of the image, likely associated with a convective band of precipitation.

Figure 7b shows that the convective band in the radar image is not identified by the algorithm. Because the convective band is not identified, it is not possible to identify features within this band. A region near the edge of the image is identified as convective. This region may have been properly identified as stratiform if it was not near the edge of the domain. Figures 7c through 7e show the structures present at the spatial scales examined. Overall, the algorithm performed poorly in this case. Structure identification performed poorly in this case due to poor performance of identifying convective and stratiform precipitation. The failure to detect the convective band within the image is likely due to the weak reflectivity gradients in and around the convective band.

8) KSGF at 0200 UTC on June 14, 2005

A curved broken line of thunderstorms extends from the southwest corner to the northeast corner of the image, shown in figure 8a, with additional thunderstorms located near the center of the image. Little stratiform precipitation is observed. Weaker echoes are noted in the vicinity of reflectivity cores and are likely due to thunderstorm anvils.

The classification of convective and stratiform precipitation, shown in figure 8b, is reasonable. Figures 8c through 8e show the structures present at the spatial scales examined. Some cells that are small and close together in the image are identified as one elongated cell when they should be identified as multiple cells. However, the identification of segments and clusters within the image is reasonable. The performance of the algorithm at identifying convective and stratiform precipitation was very good. The algorithm performed moderately well at identifying features of multiple scales within the image.

9) KSGF at 0330 UTC on June 26, 2003

In figure 9a, a broken line of thunderstorms extends north and east from the southwest part of the image through the northeast part of the image. Large region of stratiform precipitation is present to the north and west of the line of thunderstorms. Some convective cells are embedded within the stratiform precipitation and possibly along the northwest edge of the stratiform precipitation.

Although it appears in figure 9b that all convective features are properly identified, some stratiform regions are also identified as convective. Figures 9c through 9e show the structures present at the spatial scales examined. Many small cells are not identified within the image. Identification of segments and clusters appears more reasonable. However, there are regions that do not appear particularly convective in nature that are identified as segments. The algorithm performed moderately well at identifying convection and stratiform precipitation. The performance of identifying features of multiple scales was moderate.

10) KSGF at 1900 UTC on December 6, 2007

Figure 10a shows a large area of stratiform precipitation is spread over almost the entire domain. The heaviest precipitation is spread over the southern portion of the domain. Much of the precipitation is frozen during this event. No convection is obvious within the domain.

As shown in figure 10b, most of the image is correctly identified as stratiform precipitation. The regions identified as convective may be false positives. Figures 10c through 10e show the structures present at the spatial scales examined. No cells are identified within the image. However, considering that the precipitation is stratiform in nature, the identification of a segment and cluster is not reasonable. The performance was moderately good at identifying convective and stratiform precipitation. Identification of structures within the image was moderately poor. Had no convection been identified, there would not be structures to the identify, and the algorithm would have exhibited better performance.

8. ANALYSIS OF RESULTS

The algorithm generally performed quite well over the selected cases in identifying convective and stratiform precipitation. Although there were a few false positives and missed regions of convection, nearly all convective and stratiform precipitation was correctly identified. In the cases where convective and stratiform precipitation did not appear to be identified correctly, the precipitation was marginally convective or stratiform. In cases of obvious convection and obvious stratiform precipitation, the algorithm performed very well.

Larger features appeared to be identified more correctly than smaller features. Although many cells were identified correctly, too few cells were identified by the algorithm. One common problem was the identification of two or more nearby cells identified as a single cell. Generally, identification of segments and clusters was done well. However, at times, features that appeared to be too small to qualify as a segment or a cluster were identified as such. The algorithm performed better in identifying larger features than it did in identifying smaller features. Discrete cells and cells within clusters that had distinct strong reflectivity cores were identified quite well.

The algorithm performance was also degraded when irregular features of a variety of spatial scales were present in the image, such as in case (8). Although the algorithm performed well under a variety of conditions, this may be a limitation of using Fourier analysis. In these cases, wavelet analysis may outperform algorithms that are based on the FT.

9. FUTURE WORK

The cell identification and classification scheme is being incorporated into a larger cell classification scheme based on cell attributes and near storm environment data (Lack and Fox 2008). When completed, the cell classification scheme will identify convective cells and calculate attributes of the convective cells to classify the cells. The cell classification can be used as part of a nowcasting scheme for the purpose of applying conceptual models to forecast cell behavior.

The identification of convective structures on multiple scales is useful in verification of output of nowcasting schemes. This algorithm delineates convective structures on three scales, which may be useful in evaluating the performance of nowcasting schemes in forecasting the evolution of structures of different scales within a radar image. The classification of precipitation type can be used to select and apply different Z-R relationships to different portions of a radar image. This may improve the estimates of rainfall accumulation. Additionally, rainfall accumulation estimates generated through this method may be useful for verifying the performance of precipitation generated within numerical models.

10. CONCLUSION

Convective and stratiform regime identification is a strength of this algorithm. Although the identification of structures within an image at multiple scales did not perform as well, the issues occurred largely when convective features were small, very closely spaced, or exhibited relatively weak reflectivity. Additionally, because of the nature of the algorithm, identification of structures within the radar image depends on the identification of convective and stratiform precipitation. Some of the failures of the structure identification scheme were caused by poorly identified convection and stratiform precipitation.

Although multiscale advection of structures within a radar image has been implemented in nowcasting schemes, use of multiscale analysis is very limited in analyzing structures within a radar image. The FT, or a

similar transform, may be useful in identification and analysis of convective and stratiform structures within a radar image.

11. ACKNOWLEDGEMENTS

12. REFERENCES

Hagelberg, C. and J. Helland, 1995: Thin-line detection in meteorological radar images using wavelet transforms. *J. Atmos. Oceanic Technol.*, **12** (3), 633-642.

Klazura, G. E., J. M. Thomale, D. S. Kelly, and P. Jendrowski, 1999: A comparison of NEXRAD WSR-88D radar estimates of rain accumulation with gauge measurements for high- and low-reflectivity horizontal gradient precipitation events. *J. Atmos. Oceanic Technol.*, **16** (11), 1842-1850.

Lack, S. A. and N. I. Fox, 2008: An automated approach for identifying convective storm type using reflectivity and near-storm environment data. Preprints, *6th Conference on Artificial Intelligence Applications to Environmental Science*, Amer. Meteor. Soc., New Orleans, J4.3.

Lakshmanan, V., T. Smith, K. Hondl, G. J. Stumpf, and A. Witt, 2006: A real-time, three dimensional, rapidly updating, heterogeneous radar merger technique for reflectivity, velocity, and derived products. *Wea. Forecasting*, **21** (5), 802-823.

————, T. Smith, G. J. Stumpf, and K. Hondl, 2007: The warning decision support system – integrated information (WDSS-II). *Wea. Forecasting*, **22** (3), 596-612.

Liu, S., M. Xue, and Q. Xu, 2007: Using wavelet analysis to detect tornadoes from doppler radar radial-velocity observations. *J. Atmos. Oceanic Technol.*, **24** (3), 344-359.

Seed, A. W., 2003: A dynamic and spatial scaling approach to advection forecasting. *J. Appl. Meteorol.*, **42** (3), 381-388.

Turiel, A., J. Isern-Fontanet, and E. García-Ladona, 2007: Wavelet filtering to extract coherent vortices from altimetric data. *J. Atmos. Oceanic Technol.*, **24** (12), 2103-2119.
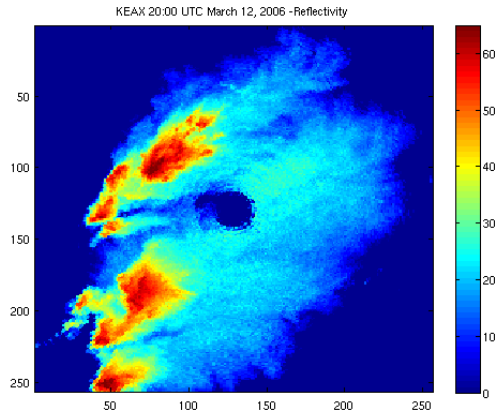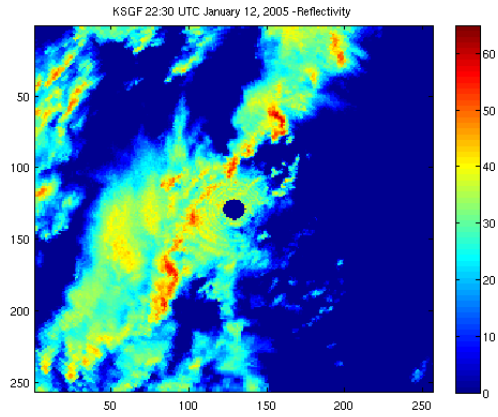
**Figure 1a:** *Radar reflectivity observed by KEAX at 20:00 UTC on March 12, 2006*
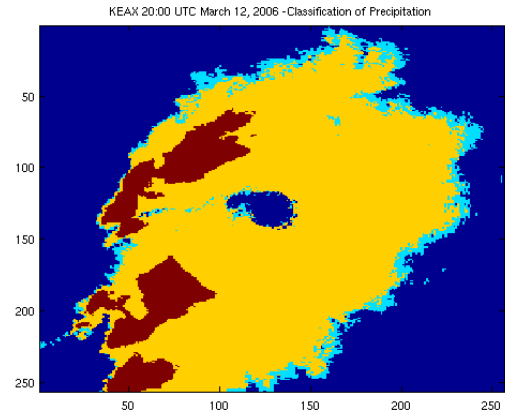
Figure 1b: *Precipitation classification for the radar image from KEAX at 20:00 UTC on March 12, 2006*
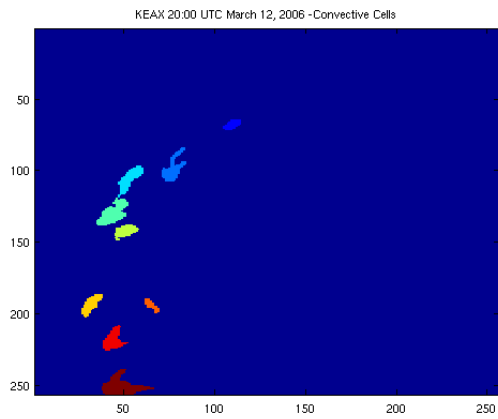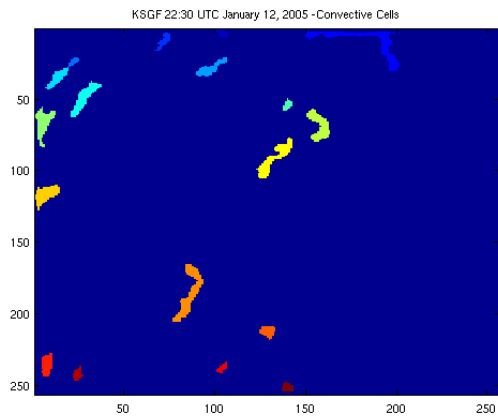

Figure 1c: *Cells identified within the radar image from KEAX at 20:00 UTC on March 12, 2006*
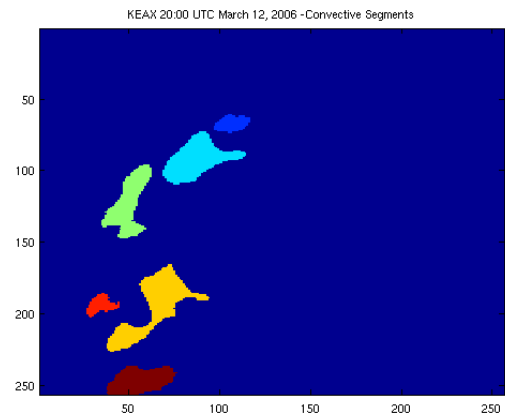
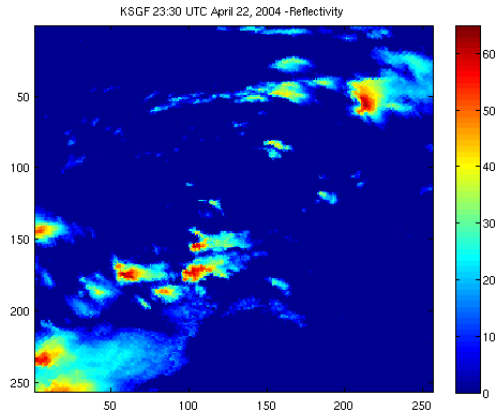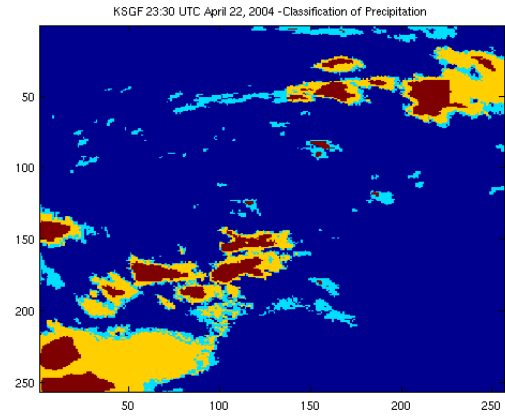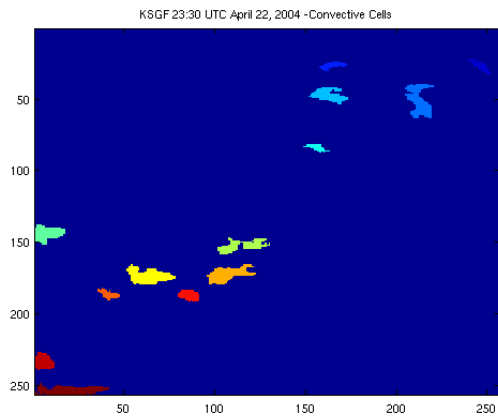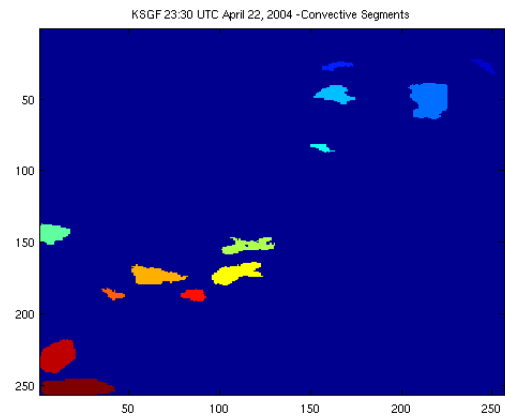**Figure 1d:** *Segments identified within the radar image from KEAX at 20:00 UTC on March 12, 2006*
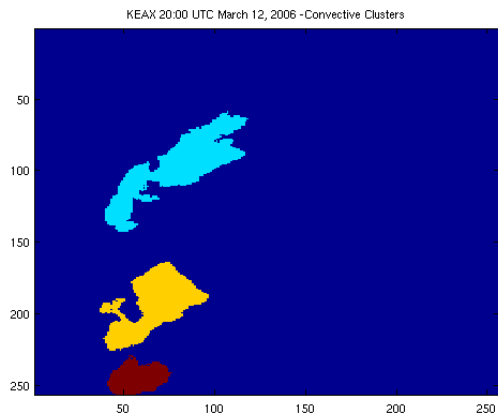
Figure 1e: *Clusters identified within the radar image from KEAX at 20:00 UTC on March 12, 2006*
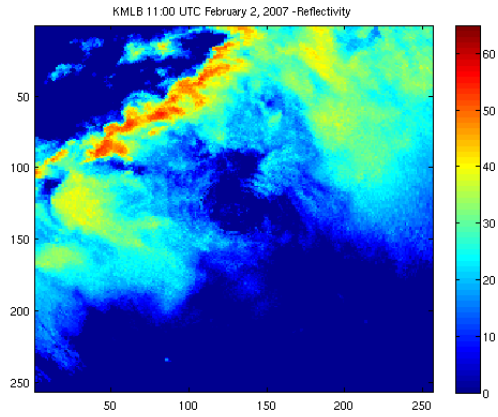
Figure 2a: *Radar reflectivity observed by KMLB at 11:00 UTC on February 2, 2007*
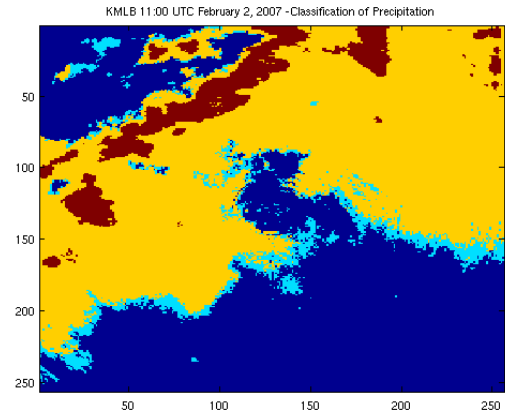
Figure 2b: *Precipitation classification for the radar image from KMLB at 11:00 UTC on February 2, 2007*
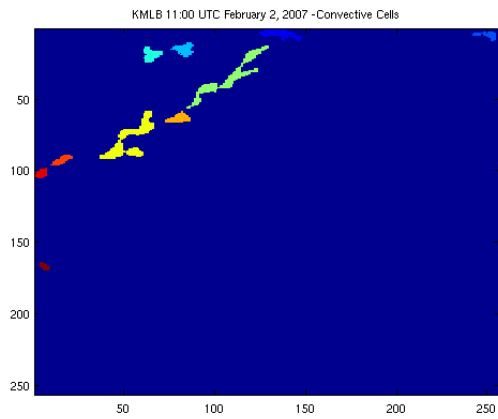
Figure 2c: *Cells identified within the radar image from KMLB at 11:00 UTC on February 2, 2007*
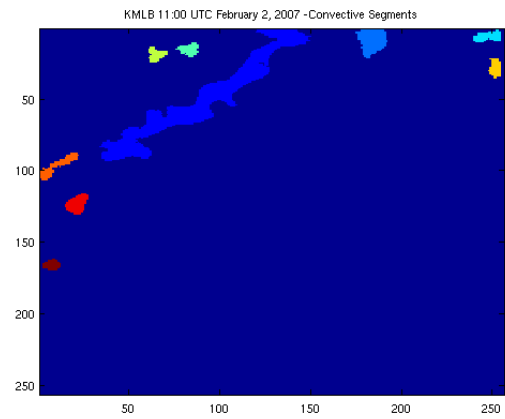
Figure 2d: *Segments identified within the radar image from KMLB at 11:00 UTC on February 2, 2007*
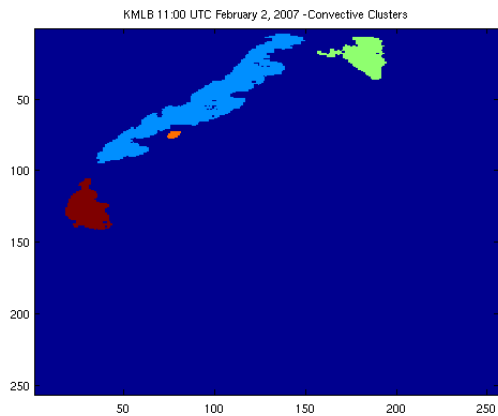
Figure 2e: *Clusters identified within the radar image from KMLB at 11:00 UTC on February 2, 2007*
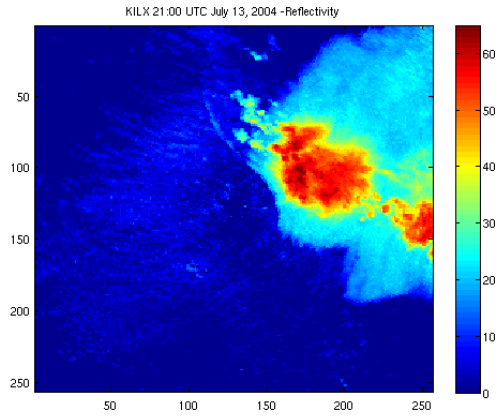
Figure 3a: *Radar reflectivity observed by KILX at 21:00 UTC on July 13, 2004*
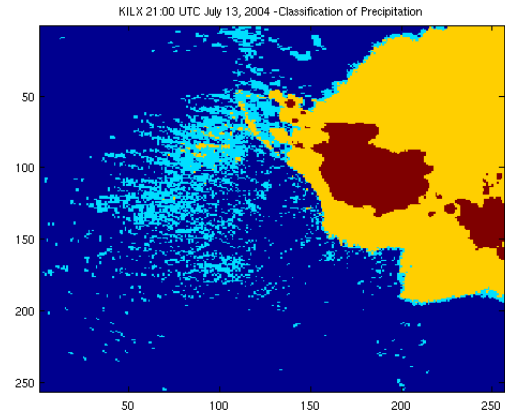
Figure 3b: *Precipitation classification for the radar image from KILX at 21:00 UTC on July 13, 2004*
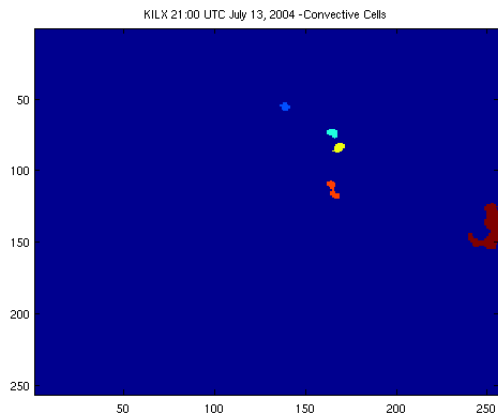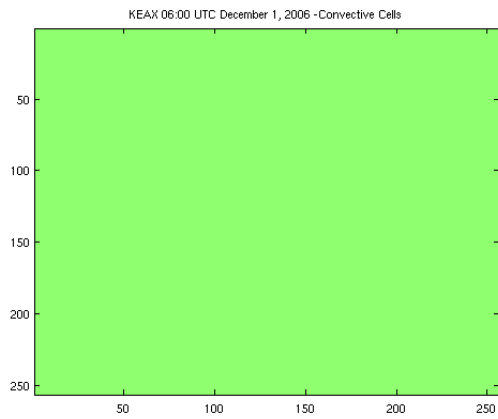

Figure 3c: *Cells identified within the radar image from KILX at 21:00 UTC on July 13, 2004*
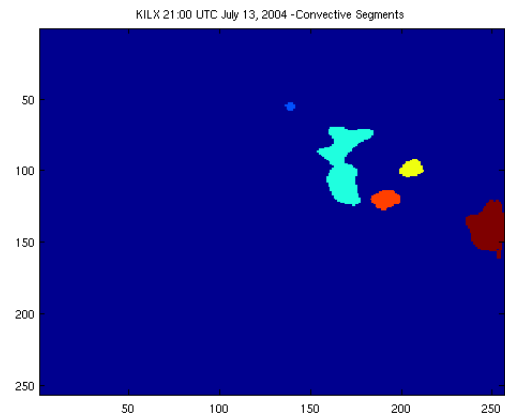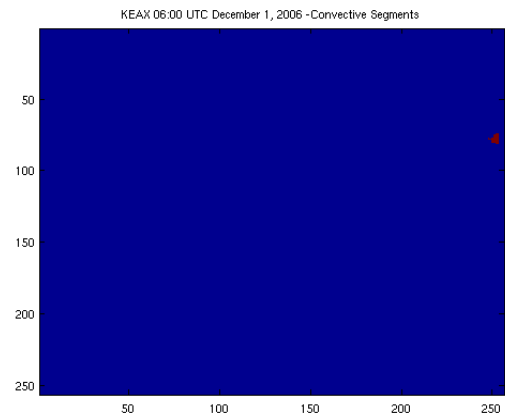

Figure 3d: *Segments identified within the radar image from KILX at 21:00 UTC on July 13, 2004*
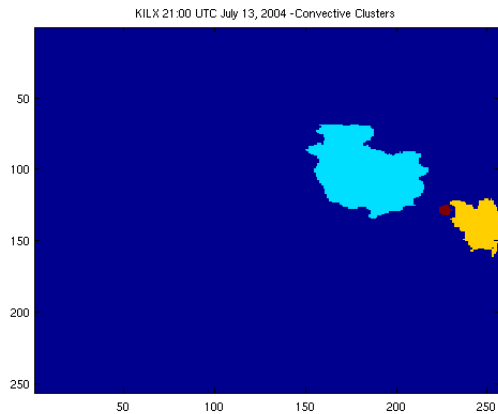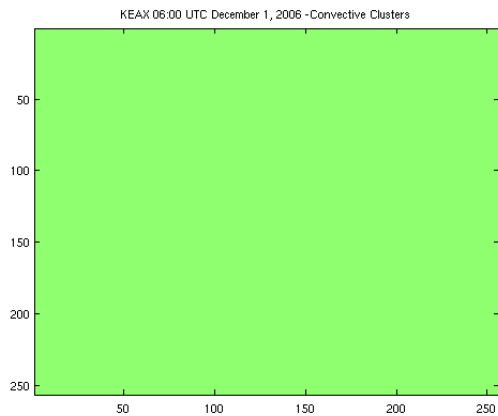

Figure 3e *Clusters identified within the radar image from KILX at 21:00 UTC on July 13, 2004*
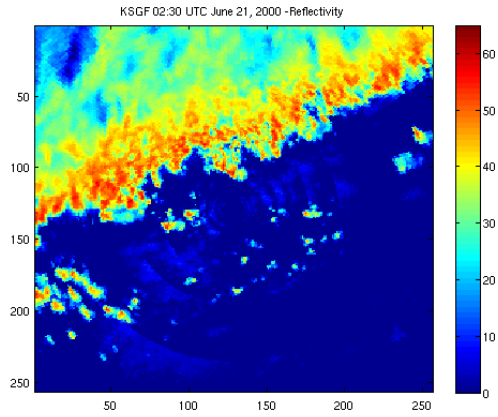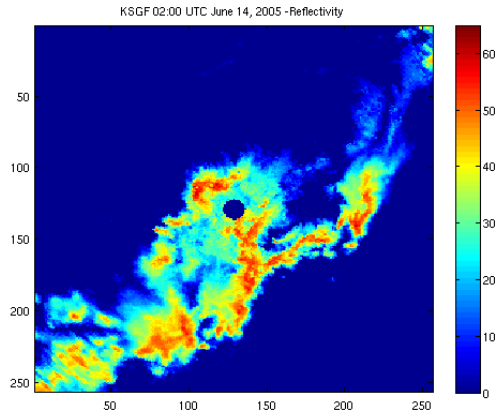
Figure 4a: *Radar reflectivity observed by KSGF at 02:30 UTC on June 21, 2000*
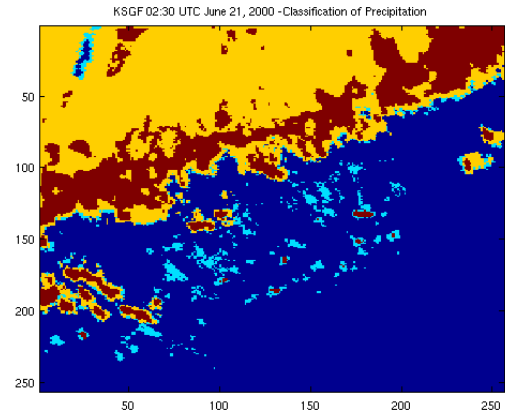
Figure 4b: *Precipitation classification for the radar image from KSGF at 02:30 UTC on June 21, 2000*
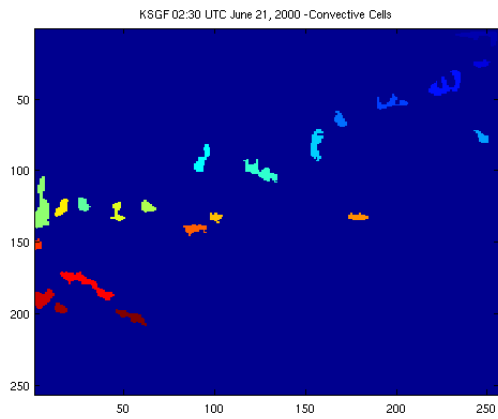
Figure 4c: *Cells identified within the radar image from KSGF at 02:30 UTC on June 21, 2000*
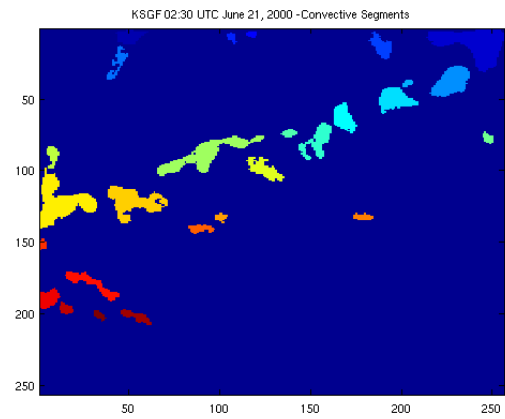
Figure 4d: *Segments identified within the radar image from KSGF at 02:30 UTC on June 21, 2000*
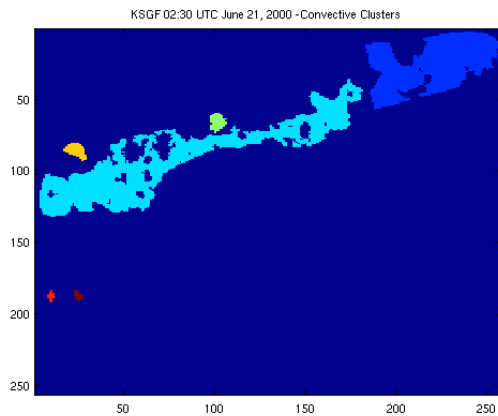
Figure 4e: *Clusters identified within the radar image from KSGF at 02:30 UTC on June 21, 2000*

Figure 5a: *Radar reflectivity observed by KSGF at 22:30 UTC on January 12, 2005*
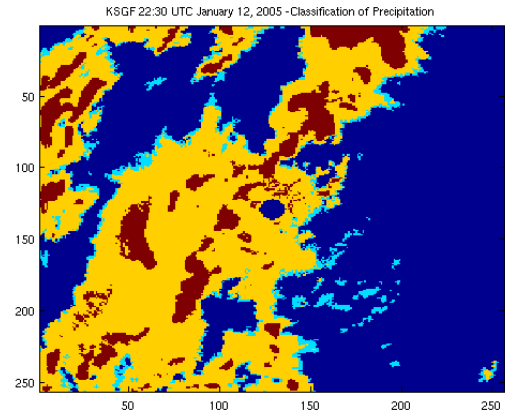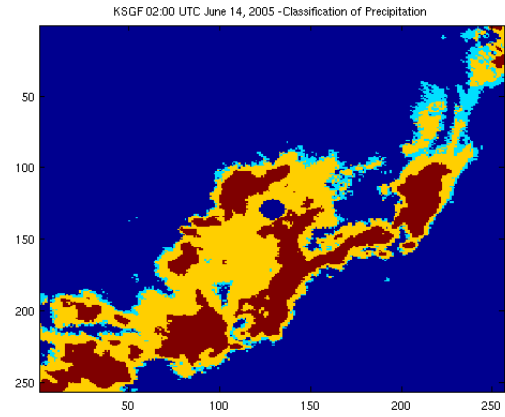

Figure 5b: *Precipitation classification for the radar image from KSGF at 22:30 UTC on January 12, 2005*
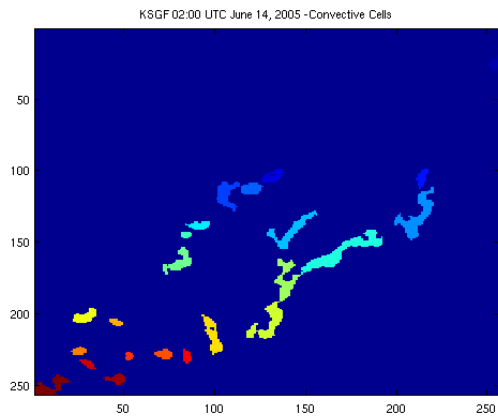

Figure 5c: *Cells identified within the radar image from KSGF at 22:30 UTC on January 12, 2005*
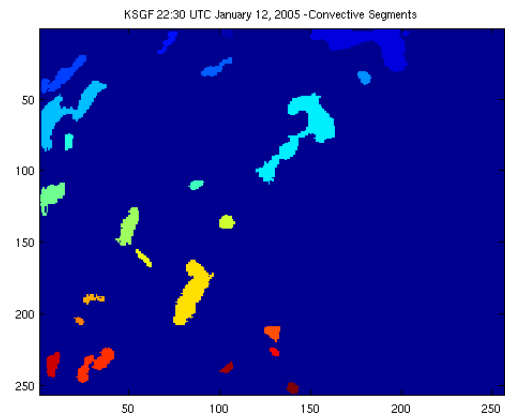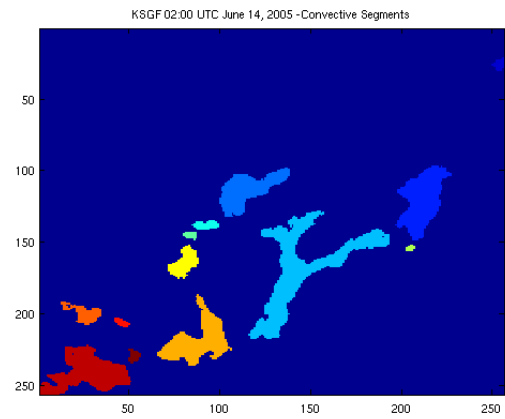

Figure 5d: *Segments identified within the radar image from KSGF at 22:30 UTC on January 12, 2005*
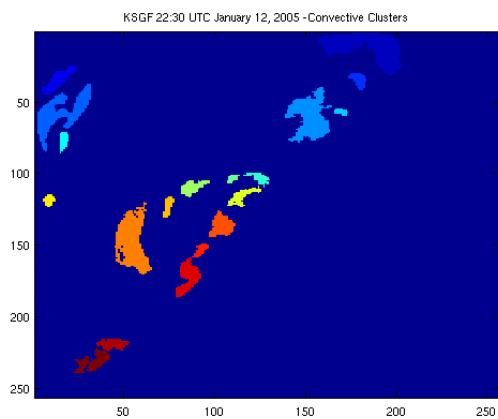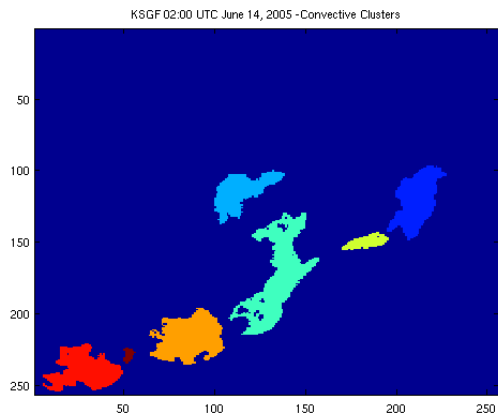

Figure 5e: *Clusters identified within the radar image from KSGF at 22:30 UTC on January 12, 2005*
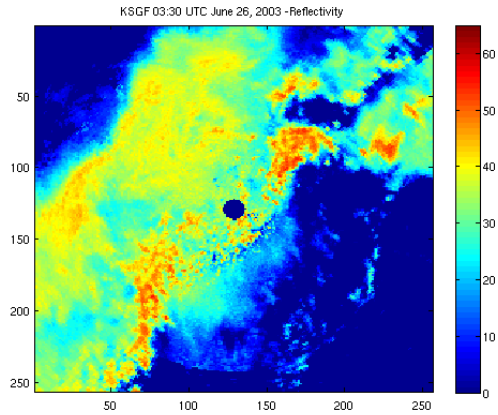
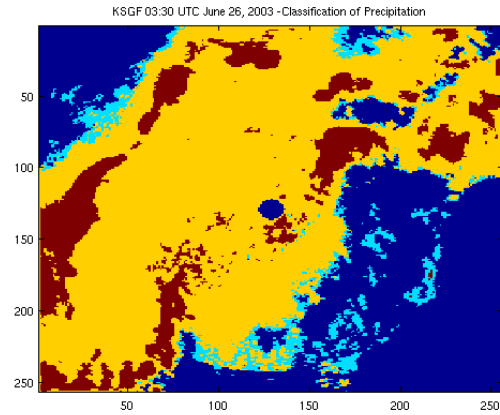**Figure 6a:** *Radar reflectivity observed by KSGF at 23:30 UTC on April 22, 2004*

Figure 6b: *Precipitation classification for the radar image from KSGF at 23:30 UTC on April 22, 2004*

Figure 6c: *Cells identified within the radar image from KSGF at 23:30 UTC on April 22, 2004*

Figure 6d: *Segments identified within the radar image from KSGF at 23:30 UTC on April 22, 2004*
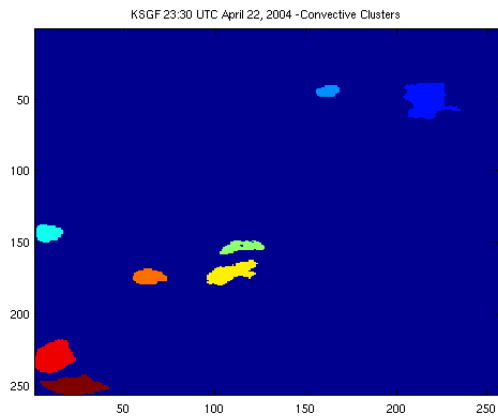
Figure 6e: *Clusters identified within the radar image from KSGF at 23:30 UTC on April 22, 2004*
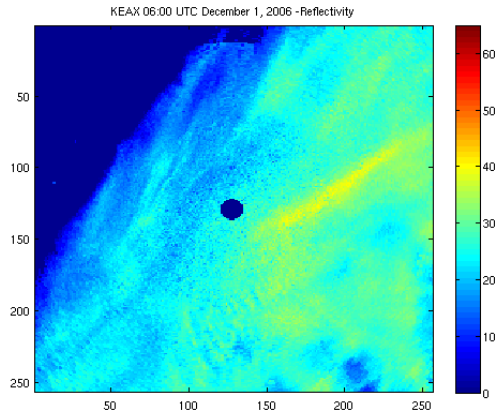
Figure 7a: *Radar reflectivity observed by KEAX at 06:00 UTC on December 1, 2006*
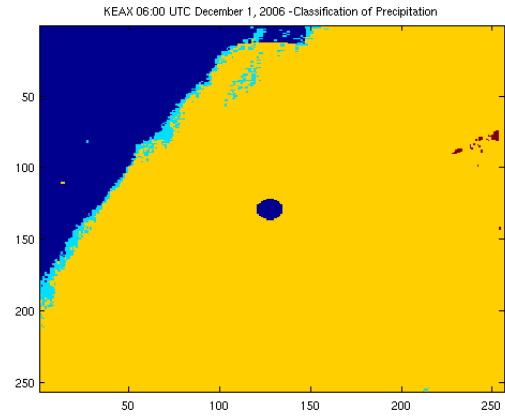
Figure 7b: *Precipitation classification for the radar image from KEAX at 06:00 UTC on December 1, 2006*

Figure 7c: *No cells identified within the radar image from KEAX at 06:00 UTC on December 1, 2006*

Figure 7d: *Segments identified within the radar image from KEAX at 06:00 UTC on December 1, 2006*

Figure 7e: *No clusters identified within the radar image from KEAX at 06:00 UTC on December 1, 2006*

Figure 8a: *Radar reflectivity observed by KSGF at 02:00 UTC on June 14, 2005*

Figure 8b: *Precipitation classification for the radar image from KSGF at 02:00 UTC on June 14, 2005*
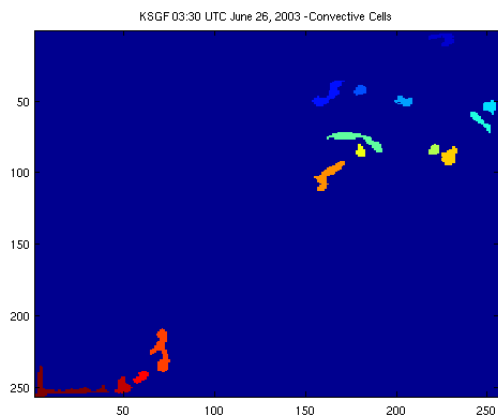

Figure 8c: *Cells identified within the radar image from KSGF at 02:00 UTC on June 14, 2005*
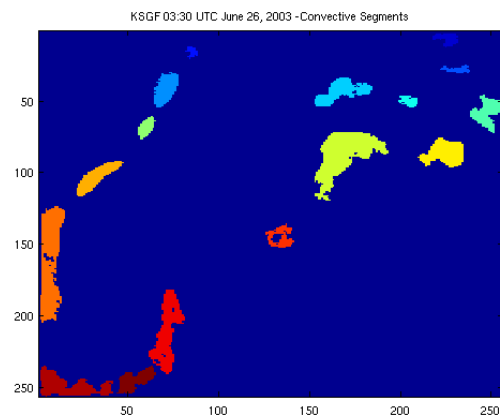

Figure 8d: *Segments identified within the radar image from KSGF at 02:00 UTC on June 14, 2005*

Figure 8e: *Clusters identified within the radar image from KSGF at 02:00 UTC on June 14, 2005*

Figure 9a: *Radar reflectivity observed by KSGF at 03:30 UTC on June 26, 2003*

Figure 9b: *Precipitation classification for the radar image from KSGF at 03:30 UTC on June 26, 2003*

Figure 9c: *Cells identified within the radar image from KSGF at 03:30 UTC on June 26, 2003*

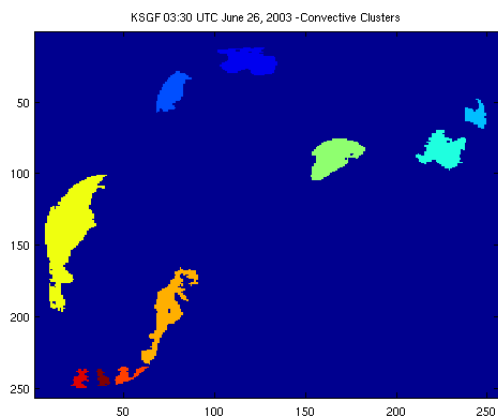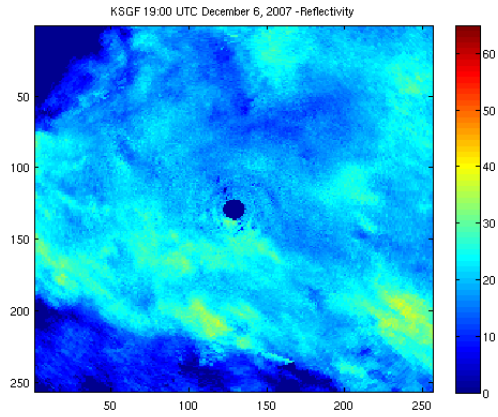**Figure 9d:** *Segments identified within the radar image from KSGF at 03:30 UTC on June 26, 2003*

Figure 9e: *Clusters identified within the radar image from KSGF at 03:30 UTC on June 26, 2003*

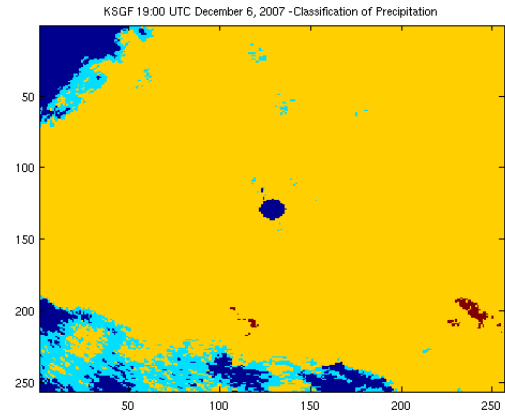**Figure 10a:** Radar reflectivity observed by KSGF at 19:00 UTC on December 6, 2007

Figure 10b: Precipitation classification for the radar image from KSGF at 19:00 UTC on December 6, 2007
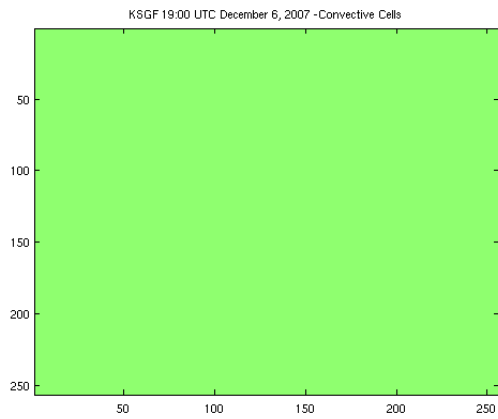

Figure 10c: No cells identified within the radar image from KSGF at 19:00 UTC on December 6, 2007
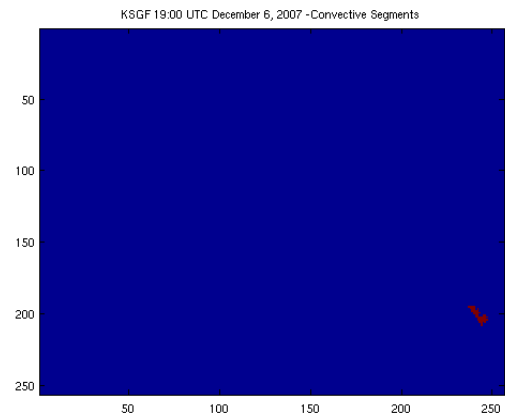

Figure 10d: Segments identified within the radar image from KSGF at 19:00 UTC on December 6, 2007
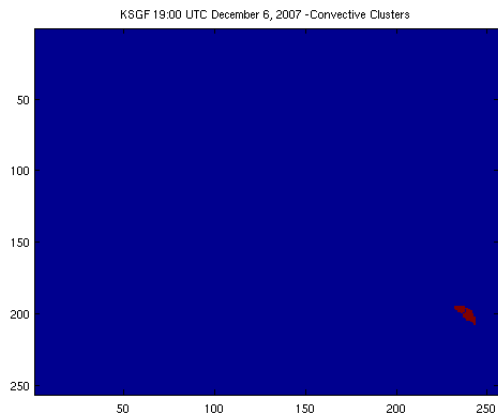

Figure 10e: Clusters identified within the radar image from KSGF at 19:00 UTC on December 6, 2007